# Influence of gaseous environment on the properties of Inconel 625 L-PBF parts

S. Traoré [a], I. Koutiri [a], M. Schneider [a], P. Lefebvre [b], J. Rodrigues [a], C. Dupuy [a], F. Coste [a], P. Peyre [a,*]

[a] *PIMM Laboratory, Arts et Métiers Institute of Technology, CNRS, CNAM, HESAM University, 151 Bd de l'Hôpital, 75013 Paris, France*
[b] *Air Liquide Campus Innovation, 1 Chemin de la Porte des Loges, 78350 Les-Loges-en-Josas, France*

### A B S T R A C T

The effect of gaseous atmosphere during Laser Powder Bed Fusion (L-PBF) was analysed on an Inconel 625 alloy. The bead dimensions, the surface finish, the porosity rate and the resulting microstructure were analysed for three different gases (Argon, Nitrogen and Helium) in an industrial L-PBF machine, using rather high energy density promoting keyhole welding regime. No clear effect of gas nature on energy coupling was shown when considering fusion beads on L-PBF parts. However, this work shows that gas, and especially helium mostly modifies surface finish, due to a modification of heat dissipation at the interface between the built part and the powder bed. This effect is clearly beneficial for vertical builds but is balanced by a possible and detrimental reduction of surface tensions for inclined and overhanging surfaces. The data presented here indicates a moderate benefit of He and $N_2$ gases on porosity rates at high laser energy, but the as-built microstructures do not exhibit detectable differences, at the scale considered for the analyses (SEM + EBSD). Some physical aspects of the liquid/gas interface are discussed at the end of the paper to explain the observed results.

## 1. Introduction

L-PBF additive process, considered as one of the most promising manufacturing routes for obtaining dense and complex metallic parts, involves a large number of experimental parameters like laser power, scan speed, layer height, hatch distance or scan strategy. On a large range of metals or alloys, including recently pure copper as shown by [1], L-PBF allows obtaining densities superior to 99 % (<1 % porosity) but rather deleterious surface finishes with minimum average roughness Ra superior to 6–7 μm. Microstructures that result from the high-cooling rates (around $10^6$ K.s$^{-1}$) are usually fine cells or dendrites, more or less oriented parallel to the main build direction, with mostly {001} crystal textures for fcc (face-centered cubic) metals.

Recently, several authors have contributed to a better understanding of physical mechanisms induced in L-PBF such as spattering effects and denudation near the L-PBF tracks. Related works operate in instrumented set-ups to facilitate the high-speed video analysis of phenomena [2]. Experimental and numerical works indicated that denudation comes from a recirculation gas flow induced by the vertical expansion of the vapour plume [3,4]. Spatter formation was also analysed and their

evolution versus with (P, V) process conditions was evaluated qualitatively by Wang et al. [5] on a CoCr alloy, and quantitatively by Gunenthiram et al. [6] on 316L. Also, the use of time-resolved X-ray experiments at synchrotron allowed a direct and very useful side view of melt-pool instabilities, including keyhole porosities in L-PBF as shown by Zhao et al. [7].

Up to now, very few authors have considered the influence of gas shielding on L-PBF process stability and efficiency, and on resulting materials' properties. The main explanation is that most of industrial L-PBF systems only work under argon or nitrogen atmospheres. In most of the current published work on L-PBF, the machines operate under Ar shielding, which is the most common build environment, whatever the material considered. However, several gas features such as thermal conductivity K (W/m/K), density $\rho$ (kg/m$^3$) or viscosity $\eta$ (Pa. s) are assumed to play a non-negligible role either on laser-material coupling (metal vapour expansion, pollution of experimental chambers) or on thermal boundary conditions and resulting materials' properties.

In the early 2000's, a number of studies have considered the influence of various protective atmospheres during $CO_2$ or Nd:YAG laser welding, with the objective of stabilizing melt-pool dynamics, increasing

---

**Table 1**
Process parameters and build parts' dimensions.

| Parts | N°/ Name | Dimensions [mm] | P [W] | V [mm/s] | VED [J/mm³] | I [MW/cm²] |
|---|---|---|---|---|---|---|
| Squared samples | 1 & 5 | Length 10 | 200 | 750 | 64 | 4.8 |
| | 2 & 6 | Thickness 10 | 200 | 1000 | 48 | 4.8 |
| | 3 & 7 | Height 5 | 300 | 750 | 96 | 7.2 |
| | 4 & 8 | | 300 | 1000 | 72 | 7.2 |
| Walls | 1, 2, 3 angle 0° | Length 15 Height 7 Thickness 0.5 or 1 or 5 | 275 | 760 | 86 | 6.6 |
| | A, B, C angle 40° | | | | | |

penetration depths and limiting deleterious effects of the vapour plume on laser-material energy coupling.

The transmission of laser energy through a Nd:YAG vapour plume has been analysed experimentally during welding, and Greses et al. [8] concluded to a combination of scattering and diffractive effects more than absorptive mechanisms. However, attenuation levels were shown to be rather low ($<5$ %) in the vapour plume.

Ar, He and $N_2$ gas protections were also tested during Inconel 690 Nd:YAG pulsed welding [9]. The minimum porosity rate (0.5 %) was obtained with $N_2$, and the maximum (4–5 %) with Ar. As a possible explanation, authors mention: (1) a reduction of surface tensions under $N_2$ that could allow gas bubbles to escape faster from melt-pools, (2) a faster dissolution of $N_2$ bubbles in the melt-pool. The same authors also mention a huge reduction of vapour plume with He, due to its higher thermal diffusivity.

The influence of $O_2$ content in Ar, on the weld tracks shapes was also shown by Patschger et al. [10], who mentioned a step-by-step suppression of negative Marangoni flow at higher $O_2$ contents, resulting in more vertical welds.

Focusing now on more recent L-PBF works, one can distinguish between two approaches: (1) the direct analysis of L-PBF materials' properties under various protective atmospheres, (2) the physical analysis of laser-powder-melt-pool coupling under modified gas shielding.

Regarding this first approach, Rakesh et al. [11] compared the morphological, microstructural and mechanical properties of an Al10SiMg alloy fabricated with L-PBF under Ar or $H_2$ atmospheres. The main effect of $N_2$ compared to Ar was a 25 % reduction of surface roughness, but nearly similar densities (around 98.5 %), microstructures and mechanical resistance under tensile loading. However, authors did not provide clear explanations for the observed results.

For a given gas shielding, the influence of part position on the building platform, and distance to the incident crossflow is also of primary importance. For instance, Ferrar et al. [12] have shown that parts located at the higher distance from the gas flow entrance exhibited a higher porosity rate. Additionally, the L-PBF building strategy is constrained by vapour plume – laser interactions: Anwar et al. [13] indicated that scan paths parallel to and in the same direction as the gas flow favour laser-plume interactions and are not recommended in a L-PBF procedure. This explains the occurrence of forbidden scan directions (mostly parallel to the crossflow direction) in many L-PBF machines.

Reijonen et al. [14] has recently investigated the influence of argon flow velocity in a L-PBF machine on the resulting properties of a 316L steel. Below a given gas flow (around 1.5 m/s), and especially for high linear energy (P/V) conditions, the laser-metal vapour plume interaction limits energy transmission, strongly reduces penetration depth, and promotes porosity generation.

Wang et al. [15] have compared the influence of Ar, He and $N_2$ during L-PBF on Al12Si aluminum alloy. A tiny increase of porosity rate was shown with He, which resulted in a severe reduction of ductility (−50 %) during tensile testing. Authors explained this result by the occurrence of porosity clusters on all the L-PBF samples built with

helium. A similar tendency was obtained by Dai et al. [16] with a lower porosity rate on Ar than on $N_2$ and He.

A limited number of authors have considered the influence of build environment at the melt-pool scale. Traore et al. [17] have shown that the use of He instead of Ar did not modify the global dimensions of fusion tracks and hence the resulting energy coupling. However, authors observed a reduced amount of spatters, and enhanced denudation phenomena in He, as already shown earlier in [4]. The latter point was explained by ([4,18] by the numerical analysis of the vapour plume dynamics and the induced protective gas flow: under He, mostly due to the lower shielding gas density, a much faster gas flow is obtained that pushes powder particles towards melt-pool and promotes denudation. This also resulted in a higher building efficiency (=ratio between built volume and total melt volume) when considering single L-PBF tracks.

A recent work by [19] has shown that a mixture of 50 % Ar and 50 % He was a promising atmosphere for increasing L-PBF build rates on Ti6Al4V alloy, due to an improved energy coupling and a process stabilization. The use of He instead of Ar was also shown to increase metal hardness and tensile strength before and after heat treatment. According to the authors, a possible explanation could be a modification of Al vaporization under He.

In the current investigation, and following the recent comparison of He and Ar shielding at the melt-pool scale by [17] on an Inconel 625 alloy, a series of cubic or parallelepipedic specimens were manufactured by L-PBF in an industrial machine. The objective was to evaluate the influence of pure Ar, He and $N_2$ atmospheres on the morphological and microstructural properties of as-built parts. The resulting as-built samples were characterized using 3D profilometry, optical microscopy, EBSD, micro-hardness testing and X-ray diffraction.

## 2. Experimental procedure

### 2.1. Process conditions

L-PBF tests were carried out using an industrial SLM 125 HL machine from SLM Solutions Gmbh, with specific modifications of gas inputs and $O_2$ control to allow the use of a large range of gas, including He. For more precise data, the gas flow configuration inside the SLM125 HL chamber is well detailed in a recent publication by [14].

The main L-PBF process condition (P, V) are summarized in Table 1, for cubes, walls and cylinders. The corresponding volume energy density (VED (J/mm³) = I / V) and laser intensity (I (MW/cm²) = P (W) / $S_{laser}$ (cm²)) values are also reported. As a reminder, the VED considered in the current work (=I / V) is different from VED classically used in most of L-PBF works (called here VED*), which considered another formulation including hatch distance and layer height (VED* = P / (V. Δh • H). Such a VED formulation, considering laser diameter D, is mainly derived from analytical welding models that consider instantaneous laser-matter interaction [20], and establish a direct link between normalized penetration depth and VED.

For all these tests, the following process parameters were kept constant:

- A back-and-forth (zigzag) stripe scanning strategy for all the hatching areas, with a hatch distance of H = 120 μm,
- a 33° rotation between layers and a constant laser beam diameter of D ~ 73 μm at $1/e^2$ (estimated using a beam analyser through the determination of the laser caustic)
- a Δh = 50 μm layer height (=building platform shift)
- A 10° angle of 3D samples versus recoater direction (Fig. 1a)

Specific $O_2$ probe systems were also installed, together with high speed imaging of the process (Fig. 1b).

To ensure a nearly similar protection against oxidation, the inward gas flows $V_{gas}$ were adapted, depending on the gas density (Fig. 2). This resulted in rather similar dynamic pressure $\rho V_{gas}^2$ between Ar and He
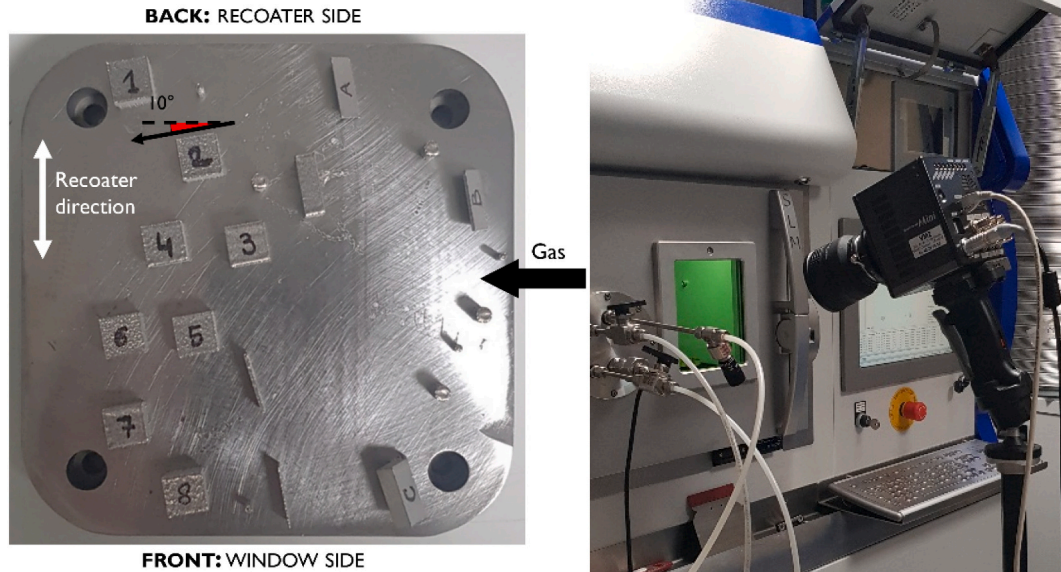
**Fig. 1.** (a) Standard build plate manufactured on the SLM 125 HL machine for the analysis of shielding gas effect, (b) $O_2$ probe systems installed in the machine and high speed imaging through the processing window.
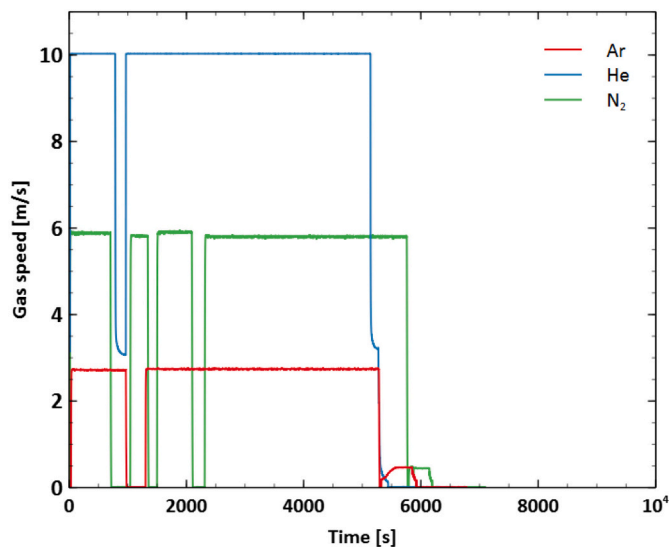


**Fig. 2.** Inward gas speeds for Ar, He, $N_2$ in the L-PBF machine chamber.

(around 13 Pa) and a somewhat higher pressure (30 Pa) for $N_2$ using recommended conditions.

The gas disruptions observed in Fig. 2 are not systematic. They have been obtained only in the case of external gas extractions (through the device shown in Fig. 1b) to measure local $O_2$ contents. Therefore they have not been considered as influent on the final properties.

### 2.2. Material and material characterization

The used Inconel 625 powder is similar to the one used in a recent publication by [17] with a chemical content of 63.8 Ni - 22.16 Cr – 9.2 Mo – 3.67 (Nb + Ta) – 0.3 Fe – 0.3 Co (with Si, C, Mn, P, S < 0.05 %), and powder grain diameters of $d_{10} = 11$ μm, $d_{50} = 25$ μm and $d_{90} = 42$ μm.

The analysis of surface roughness was made with a Dektak 150 Stylus profilometer on 3 mm × 3 mm windows and a 2.5 μm tip radius. Vickers microhardness tests were performed using a Clemex set-up, with a 200 g loading force, and with a 300 μm spacing between indentations. The

microstructures were examined by optical microscopy, and scanning electron microscopy (Philips XL 40 SEM-FEG) after immersion in a dedicated chemical etching containing 92 % HCl, 5 % $H_2SO_4$ and 3 % $HNO_3$ during 30 to 50 s. EBSD analysis were carried out on a SEM-FEG ZEISS Supra 55 VP at ICMMO (Orsay, France). Last, X-ray diffraction tests were carried out, following a similar procedure to the one described in [21] in order to estimate second and third order stresses (work-hardening) through the measurement of X-ray peaks' broadening. A X'PERT PANalytical θ-2θ goniometer was used, with a copper anticathod ($\lambda_{Cu} = 0,154,184$ nm), and a X-ray collimated spot of 2.5 mm in diameter on the analysed sample.

## 3. Influence of gas shielding on bead's dimensions

Our recent work [17] has shown a limited effect of gas shielding on single L-PBF tracks. However, when building 3D samples, the heat accumulation during additive manufacturing combined with a possible change in thermal dissipation in the surrounding gas can affect the global shapes and sizes of L-PBF tracks. To address this aspect, the last layer of the cubic L-PBF samples built in Ar, He or $N_2$ atmospheres was analysed after chemical etching, with a specific positioning of the hatching direction perpendicular to one of the side faces (Fig. 3). A comparison with single tracks is shown in Fig. 4 for Ar shielding. That simple comparison clearly indicates an increase in bead dimensions (width and height) on the 3D sample, where the keyhole welding mode is more pronounced for similar (P, V) values because of pre-heating effects. This oversizing of beads is moderate at low VED (48 J/mm³) but increases up to +20 % on widths and heights for higher VED, as shown in Fig. 5. On the other hand, considering the scattering on experimental data, an influence of gas nature on beads size is not clearly observed, whatever the configuration (single tracks or 3D samples). This tends to confirm that the modification of the shielding gas thermal properties, even with a factor 9 increase of thermal diffusivity between Ar and He, does not play a significant and dominant role on melted zones.

## 4. Analysis of surface roughness

The surface finish of as built parts is an important criterion to consider in order to limit the post-processing steps.

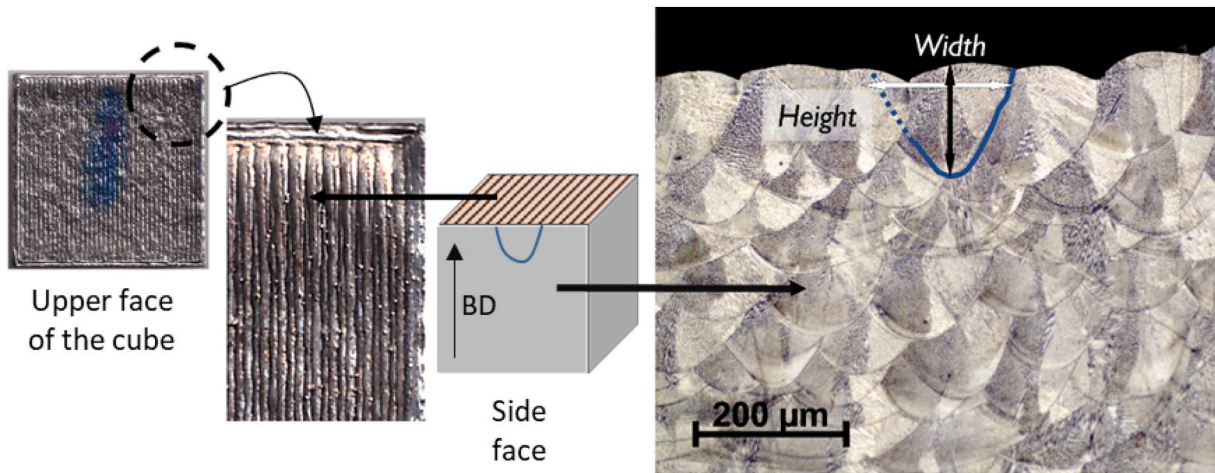In L-PBF, the arithmetic average surface roughness Ra (Eq. (1)),

**Fig. 3.** Experimental analysis of beads dimensions on the last built layer.
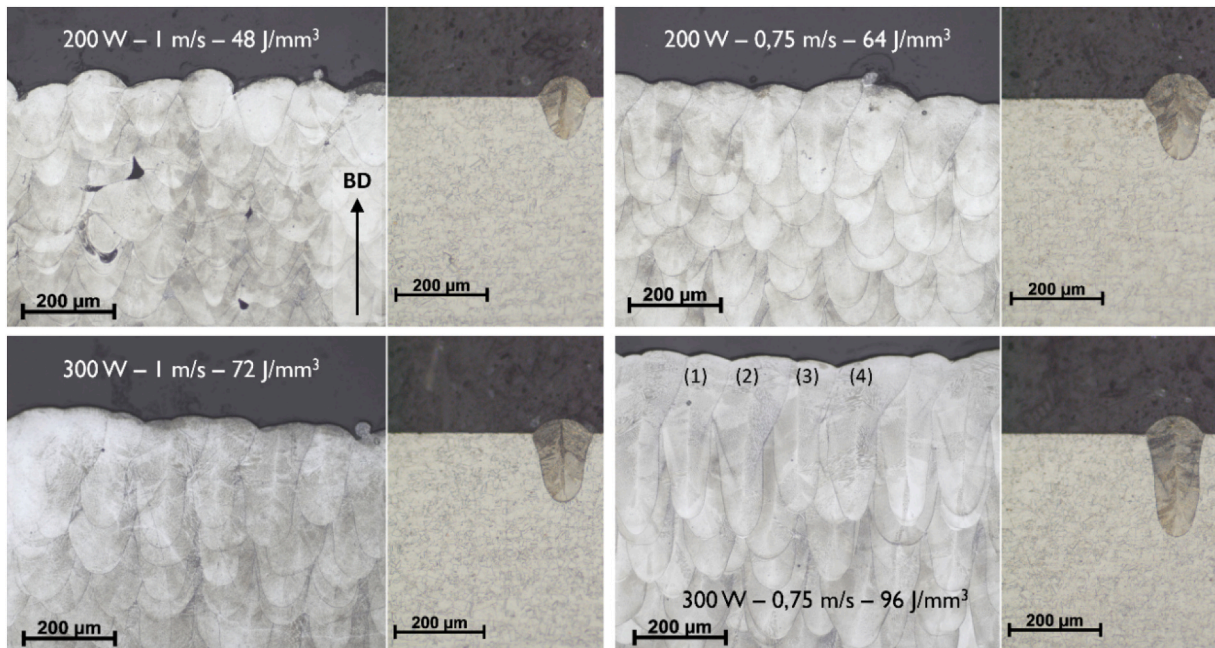


**Fig. 4.** Cross section of cubes obtained for various (P, V) conditions and comparison with single beads dimensions (Ar shielding gas), hatch distance = 120 μm.

usually superior to 6–7 μm, is mostly due to:

(1) non-melted or partially melted powder grains agglomerated on the samples' edges. Such a deleterious effect tends to increase when the wall temperature (=the surface temperature at the interface with the powder bed) is high. For this reason, smaller powder grains are supposed to improve L-PBF surface finish by limiting protrusions,

(2) a staircase effect promoted by large parts' inclinations (=large building angle versus normal direction), as modelled by Strano et al. [22].

Other features such as intense spattering can also promote high surface roughness, either on the building surface or on the lateral built sides (=sample's edges).

### 4.1. Influence of the gaseous atmosphere on surface roughness

The influence of the nature of the gas, on surface finish was evaluated by roughness measurements carried out using a mechanical profilometer (Veeco Dektak 150). The average roughness Ra and the perimeter $\tau_P$ (corresponding to the effective length scanned by the stylus and compared to the reference length: Eq. (2)) have been measured.

The corresponding analytical formulations are indicated here below:

$$R_a = \frac{1}{l} \int_0^l |z(x)| \, dx \tag{1}$$

$$\tau_p = \frac{(l_r - l)}{l} \tag{2}$$

With z(x) = distance to the average surface height, l = reference scan length, $l_r$ = recorded scan length.

For each VED, two cubes were made, one in the front of the build plate (window side) and another at the back of the build plate (scraper side: Fig. 1) in order to estimate possible discrepancies. Here, as all of the parts are identical and oriented identically on the plate, only the effect of the surface temperature will be studied. The aim is to determine the effect of thermal conductivity of gases and potential modifications of the
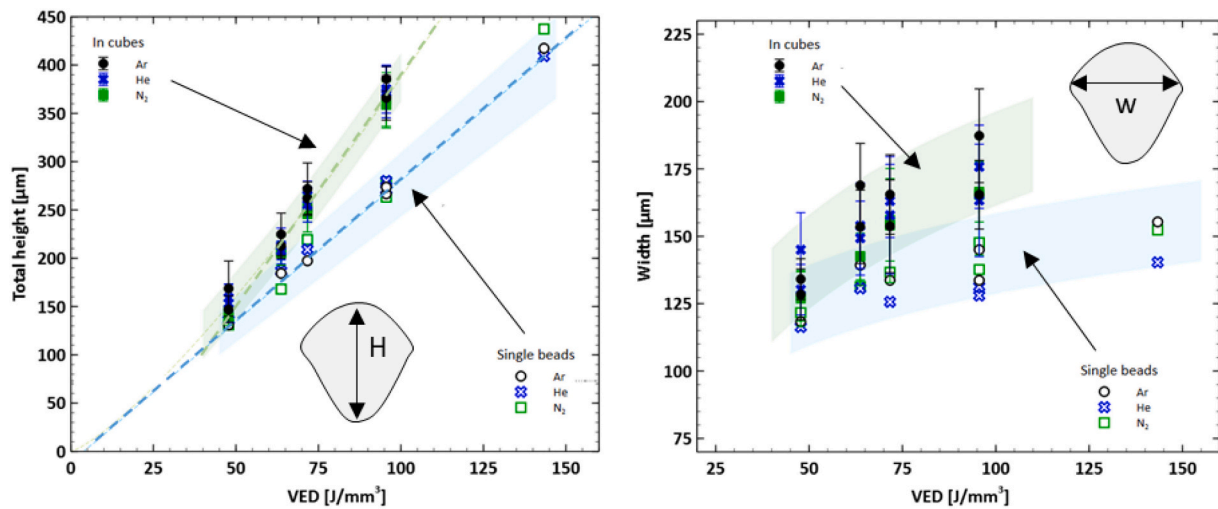
**Fig. 5.** Bead heights and widths versus VED measured on the last layer of built cubes and compared with single beads processed under Ar, He and N$_2$ atmospheres (each point corresponds to an average value for a given (P, V) condition and error bars are average deviations estimated on 3 to 4 measurements).

surface roughness.

Surface topography maps of (3000 × 3000) μm$^2$ area obtained on lateral surfaces (O, y, z) are presented in Fig. 6. The main differentiating result is that fewer powder grains are agglomerated on the surface manufactured under helium. This may reflect a larger thermal dissipation and lower wall temperature caused by the approximately 9 times higher thermal conductivity of helium compared to that of argon or nitrogen (Table 2). As the powder bed is composed of a 50 % gas – 50 % powder mixture, where the gas plays a dominant role on equivalent properties, a larger heat removal is expected under He atmosphere, which would result in fewer powder agglomerates. An additional explanation would be the reduction of spatters, widely investigated by Traore et al. [17]. The ripple pattern, linked to the superposition of layers and the resulting menisci is also less marked under He, further improving the surface finish.

The amount of powder grains on as-built surfaces under Ar and N$_2$ atmospheres seems similar. However, in the case of N$_2$, protrusions are visible on the beads, probably coming from coalesced powder grain agglomerates (about 80–90 μm in height Fig. 6) which deteriorate the average roughness of the surface. This result, and the pronounced ripple effect, may reflect a reduction of surface tension at the interface between the melt pool and the N$_2$ atmosphere which promotes capillary instabilities.

A summary of R$_a$ and τ$_P$ measurements is presented in Fig. 7. It confirms that He provides the best average surface roughness with R$_a$ between 7 and 9.5 μm, and N$_2$ shielding the larger ones ($9 < R_a < 15$ μm). As expected, the average roughness also increases with the energy density, confirming the correlation between wall temperature and surface finish.

Similar, but even clearer conclusions were obtained on the perimeter increase τ$_P$ (Fig. 7b). The contribution of peaks and valleys provokes a 6 % ± 2.5 % increase of the surface line under He, versus 12 ± 3 % under N$_2$ and 10 ± 3 % under Ar. This results in a lower specific area under He. Last, an important variability on Ra and τ$_p$ values was also observed, also depending on the location of the part on the build plate (Fig. 7). This was particularly obvious for He and N$_2$ and could be correlated to the inhomogeneous aerodynamic flow within the L-PBF chamber, and especially to the fact that the inward fluid speeds of N$_2$ and He are significantly greater than for Ar (Fig. 2).

In the LPBF process, the surface finish is generally assessed on vertical as-built (O, y, z) surfaces. However, the morphological analysis of the upper surface (O, x, y) also makes it possible to evaluate the stability of the process, the contamination by spatters, and the homogeneity of the powder layer. Some pictures recorded by a high-speed camera during the process, combined with SEM images of as-built surfaces and surface topography maps are presented in Fig. 8. This confirms that surfaces built under He are clearly smoother (Sa = 14 μm versus 20 μm with Ar and 32 μm with N$_2$), not only because of fewer liquid spatters (see high-speed images in Fig. 8) or agglomerated particles, but also because of a lower wetting angle of adjacent beads, that minimizes the amplitude of peaks and valleys.

More in detail, under argon and nitrogen, we can clearly see the periodic relief (hollows and bumps) formed by the overlap of single tracks whereas the convexity of overlapped tracks is smaller under He (SEM picture). This result could possibly reflect a modification of surface tension γ$_{LV}$ [N/m] between He and liquid Inconel 625, promoting better spreading of the liquid metal, and limiting melt-pool destabilization. Such an effect could come from a modification of the local O$_2$ rate near the build parts, as He is not considered as a chemically active and potentially surfactant gas.

### 4.2. Influence of build orientation and part thickness on surface topography

The undercut surfaces of inclined parts are areas where:

- laser heat accumulates locally because of a direct irradiation of the melt-pool powder bed interface, and because of the low equivalent conductivity of the powder bed (ten to fifty times less conductive than the solid depending on the models considered).
- surface roughness is deteriorated due to a large increase of stuck particles, and due to the melt-pool overflow when the gravity forces (F$_g$ = ρgh) exceed surface tension forces (F$_{LV}$ = γ$_{LV}$/r) holding the melt pool. The deleterious influence of stuck particles has been shown by many authors like Liu et al. [24] on 316L, Koutiri et al. [25] and Yan et al. [26] on Inconel 625, and Ladewig et al. [27] on Inconel 718.

On the one hand, due to He high conductivity, one could expect a better heat dissipation, and a possible improvement of surface finish. On the other hand, whatever the shielding gas, thinner built parts, obtained with shorter laser tracks, and surrounded by the powder bed, should favour higher local temperatures.

Three wall thicknesses of respectively 0.5 mm, 1 mm and 5 mm were considered, built either vertically or with an angle of 40° (versus the normal axis to the building plate). Similar process parameters P = 275 W and V = 760 mm/s (VED = 86 J/mm$^3$) were used.

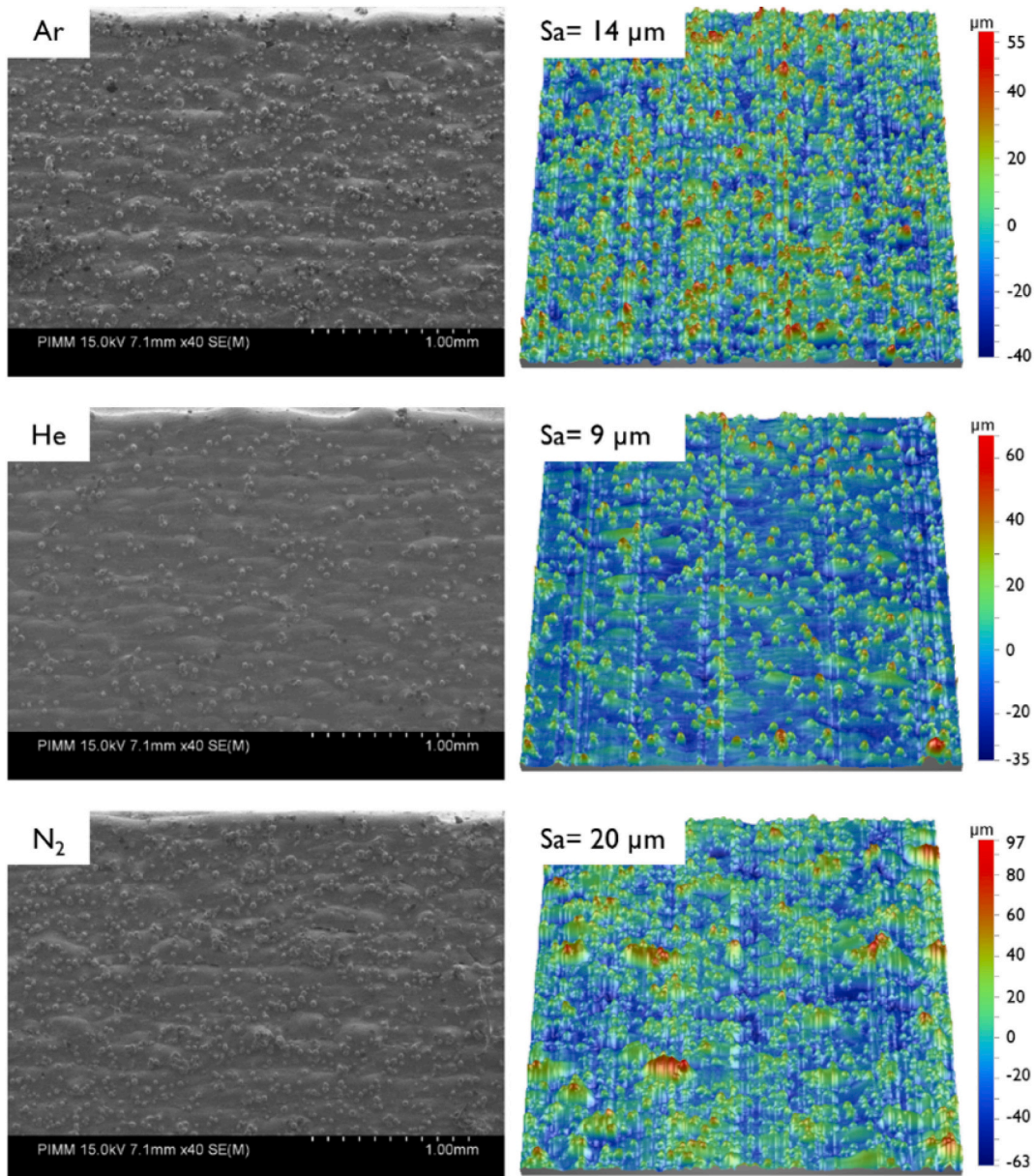Interestingly, the results shown in Fig. 9a highlight the following

**Fig. 6.** SEM images and surface topography (3 mm × 3 mm) of lateral surface of cube n°7.

| Gas | Density $\rho$ (kg. $m^{-3}$) | Thermal conductivity K ($W.m^{-1}.K^{-1}$) | Specific Heat ($J.kg^{-1}.K^{-1}$) | Thermal diffusivity ($m^2/s$) | Ionisation energy $E_i$ (eV) |
|-----|-----|-----|-----|-----|-----|
| Ar | 1.63 | 18 | 522 | 20.9 | 15.7 |
| $N_2$ | 0.97 | 26 | 1041 | 21.6 | 15.6 |
| He | 0.14 | 155 | 5190 | 183 | 24.6 |

aspects:

- There is no clear influence of the wall thickness on surface roughness, whatever the building orientation
- The beneficial effect of He observed with a normal building (0° angle) is confirmed. However, for inclined samples, surfaces are strongly deteriorated under He. For instance, Ra values, considered for underskin surfaces, tend to increase by a factor 4 or 5 (from 6 to 8 μm to 32–38 μm) with He whereas the orientation effect is smaller (~factor 2 increase on Ra) with Ar or $N_2$.

The analysis of cross-sections (Fig. 9b) reveals that the melt pool has a greater tendency to overflow under He atmosphere. This could indicate that the surface tension between He and the liquid Inconel 625 is lower than with the two other gases, with a higher Bond number (ratio between gravity and capillarity, Eq. (3)) favouring overflow.

As a reminder, the Bond number Bo compares the pressure from gravitational forces $\rho g h_{MP}$ ($h_{MP}$ = melt-pool height) with the capillary pressure $\gamma_{LV}/r_c$ for a drop (Eq. (3)). When Bo is <1, the capillary forces are dominant.

$$B_o = \frac{\rho\ g\ h_{MP}}{2\gamma_{LV}/r_c} \tag{3}$$

with: $\gamma_{LV}$ the surface tension at the liquid - vapour interface, $r_c$ the curvature radius and $h_{MP}$ the melt-pool height.
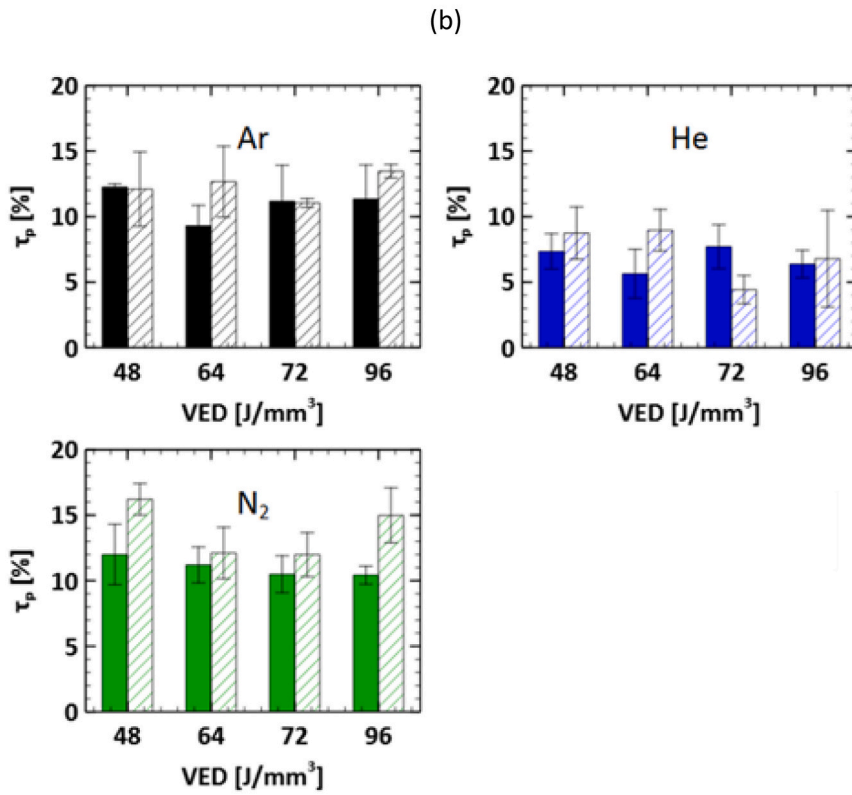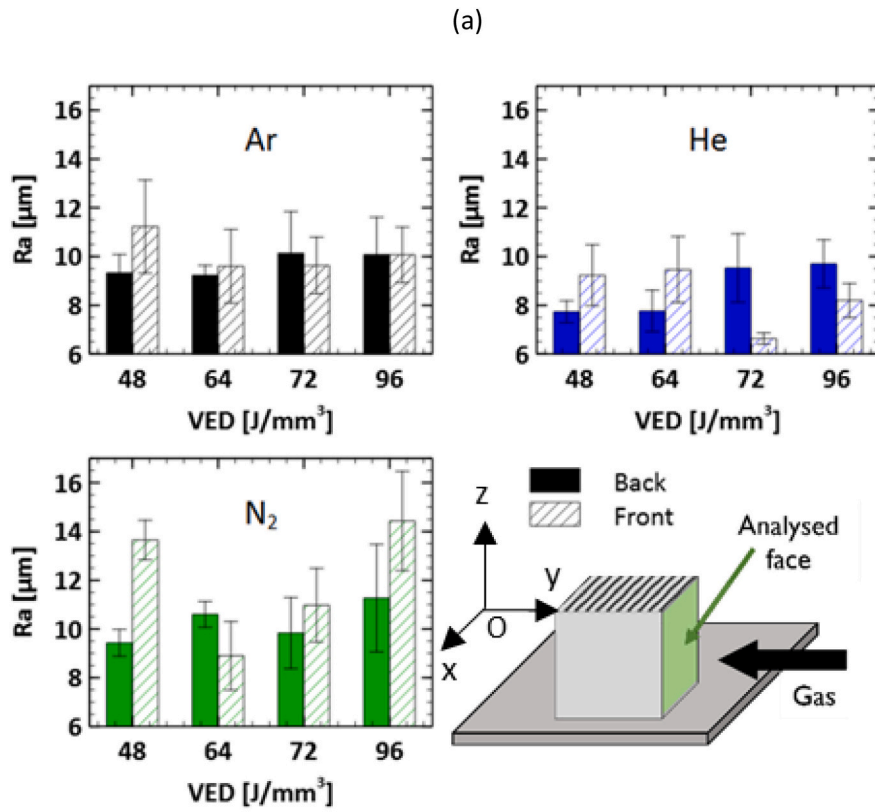
**Fig. 7.** Average Ra (a) and line perimeter $\tau_P$ (b) versus VED for Ar, He, N$_2$, and the location of parts in the L-PBF chamber (front or back position versus gas flow). Average deviations are reported as error bars.
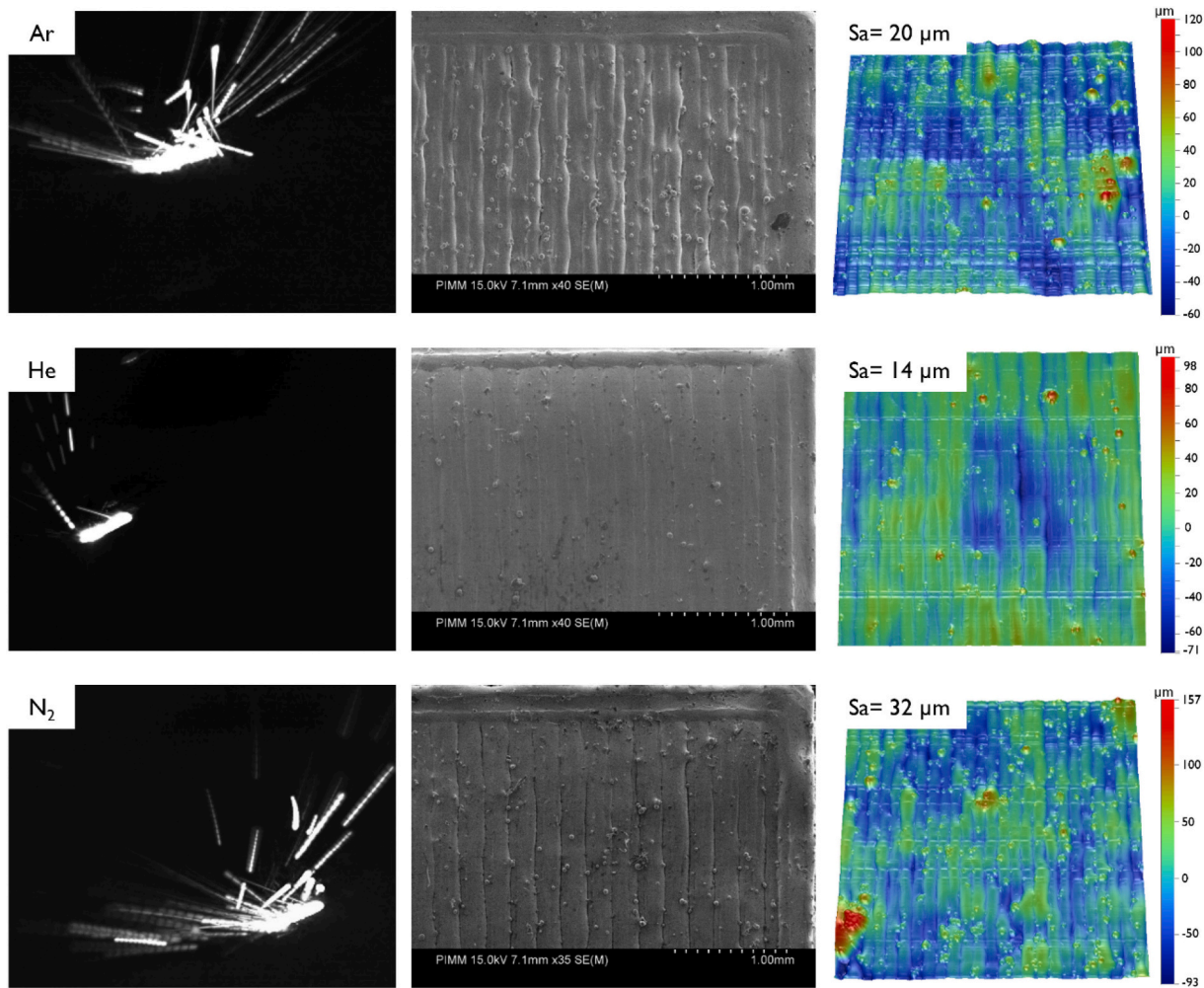
**Fig. 8.** Superposition of 10 images from high-speed videos (2000 fps) during the powder bed fusion of the cubes - SEM images and topography maps (3000 × 3000 $\mu m^2$) of the upper cube surfaces (cube n°7).

## 5. Influence of protective atmosphere on porosity rate

### 5.1. Porosity rate in cubes

Porosity rate is one of the criteria most often as an optimization criterion to select adequate L-PBF manufacturing conditions. The aim of this part is to determine whether the properties of the gas protection can influence the porosity rate in the as-built parts.

It is a well-known fact that porosities have at least the following origins:

(1) Non-spherical lacks of fusion (linked to a poor optimization of the parametric conditions) [28]
(2) An unstable keyhole welding mode (with a substantial vapour pressure deforming the melt-pool surface), promoting large and near-spherical gas cavities that cannot be removed from the melt pool before solidification [29].
(3) The occlusion of tiny gas bubbles (for instance $H_2$) coming from adsorbed water at the surface of powder grains or ambient hygrometry in the L-PBF chamber.

Possible surfactant effect (tensio-active) at the melt-pool gas interface such as those mentioned by Kuo and Lin [9] for an Inconel 690 welded in a $N_2$ atmosphere could play a beneficial role by promoting degassing effects.

In the current work, the influence of the gas nature on the porosity rate was studied on 10 mm × 10 mm × 5 mm samples for 4 distinct (P, V) conditions (Table 1). The samples were mirror polished and then observed with an optical microscope. Optical images of the whole samples cross-section, obtained at ×25 magnification are presented in Fig. 10 for two energy densities (48 and 96 J/mm$^3$) and three different gases: argon, helium, and nitrogen.

On these micrographs allowing to detect only macroscopic porosities (×25), porosities are located throughout the whole built volume at 48 J/mm$^3$, while at 96 J/mm$^3$ they are fewer, mostly localized in the contours and look like keyhole pores. Such edge effects, reported by many authors, have been attributed to:

(1) The presence of a turnaround point of the laser beam due to the back-and-forth strategy which creates local overheating (cooling time is shorter) and deeper tracks;
(2) A bad skywriting optimisation: the local scan speed at the beginning of scan tracks is then lower than the set point, provoking an excessive local VED;
(3) Specific thermal boundary conditions (powder bed poorly conductive on one of the edges) which promotes heat concentration.

These three conditions tend to promote the formation of keyhole porosities. To overcome these edge effects, the images used for the analysis of the porosity rate were taken from the core of the specimen with eight images taken at higher magnification (×200) allowing to
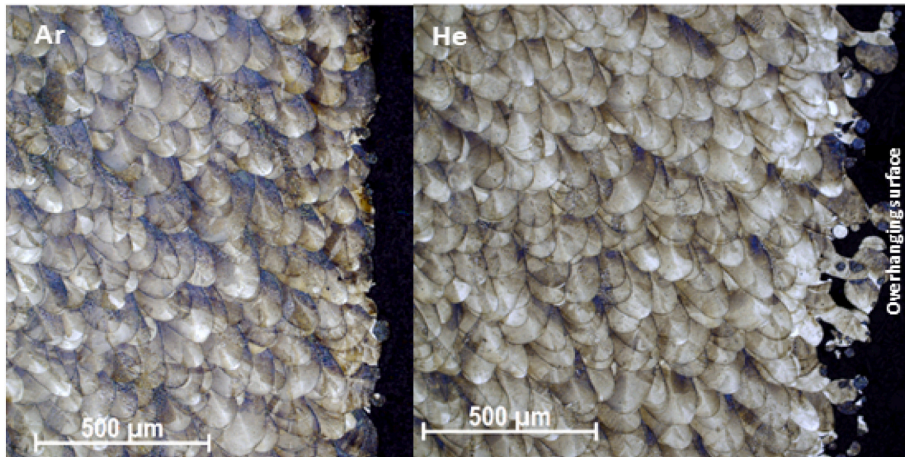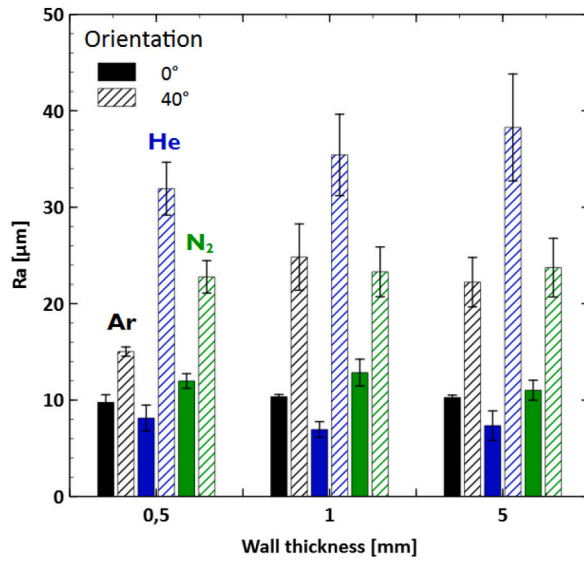
**Fig. 9.** (a) Evolution of roughness with the wall thickness and the part orientation (0° or 40°) for the three studied atmospheres Ar, He and N₂ (Average deviations are reported as error bars), (b) micrographs of underskin surfaces in Ar or He.
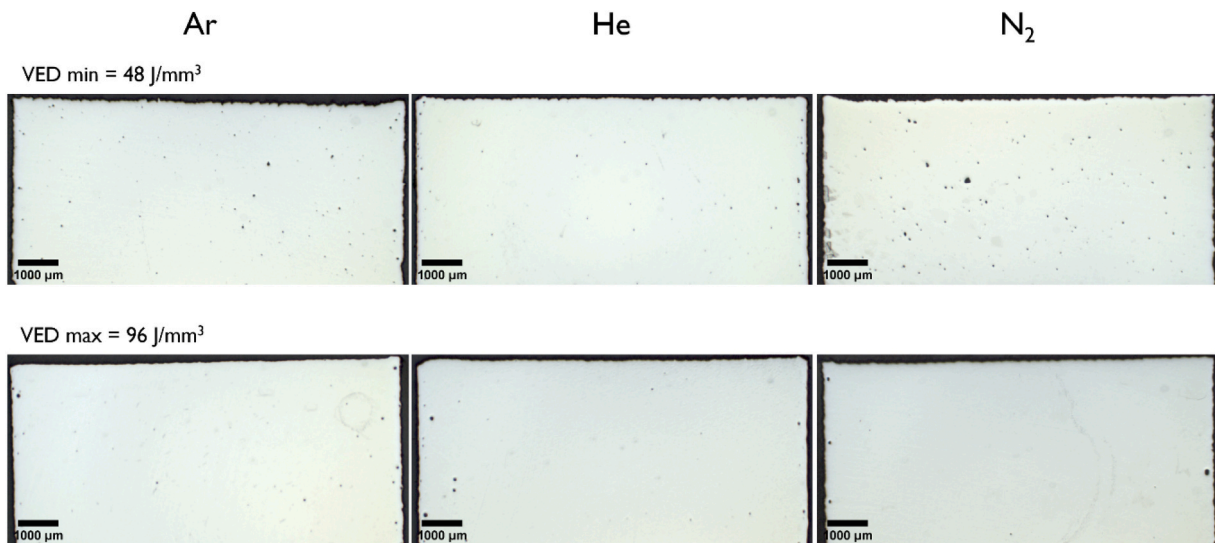


**Fig. 10.** Cross-sectional analysis (×25) of samples manufactured under Ar, He and N₂ atmospheres.
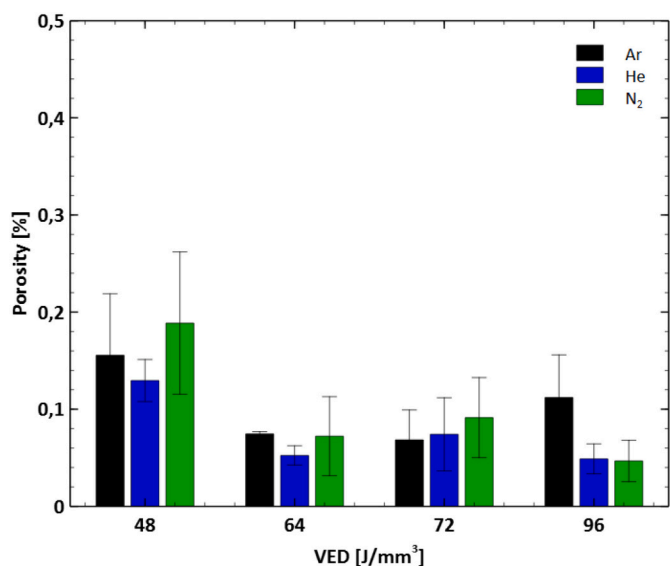
**Fig. 11.** Evolution of porosity with the VED measured in the cubes for the three studied gases.

observe smaller pores (down to 3 μm).

For the three gases, the evolution of the porosity rate as a function of the VED, is presented in Fig. 7. The porosity rates vary between 0.04 and 0.25 %, and tend to decrease with VED. Globally, except at high VED (96 J/mm³) for which Ar induces a two times higher porosity rate than with $N_2$ and He, the densification does not clearly vary with gas nature. Above 64 J/mm3, the porosity rate remains globally similar, with an average 0.05 % value. Moreover, 95 % of the detected porosities have a diameter of <10 μm, whatever the shielding gas.

### 5.2. Influence of the part size and building angle

The aim of this section is to focus on the effect of the size (specifically the width of the specimen) and the inclination of the parts with the building plate. The variation in the width of parts manufactured for the same energy conditions (275 W – 600 mm/s) makes it possible to consider different thermal boundary conditions during the build. Thus, in the thinnest walls (0.5 mm), the heat dissipation is likely to be lower since the built volume is small and completely surrounded by a powder bed which has weak thermal conductive properties. However, the nature of the gas constituting the working atmosphere, and approximately 50 % of the bed volume can modify the heat dissipation conditions at the part walls. The aim is also to see if the manufacturing angle of the part (here 40° relative to the vertical) has an effect on the porosity rate. Optical microscopy images of the samples are shown in Fig. 12 for the three widths and the two building angles.

Contrary to our expectations, more porosities are detected in thin walls (Fig. 12a). This can be explained by a higher (contour area/total built area), combined with the localization of porosities near the contour zones. Globally, similar porosity rate is obtained within the hatching areas, but the increase in specific surface (built surface over built volume) for thin samples, promotes a higher porosity rate.

Additionally, the thin and inclined parts (0.5 mm, 40°) built under helium atmosphere exhibit a less pronounced thermal distortion (curvature) than under argon (Fig. 12b). This traduces a lower thermal gradient between the undercut (down-skin) side and the upper side of the wall, which is made possible by the higher thermal dissipation in helium.
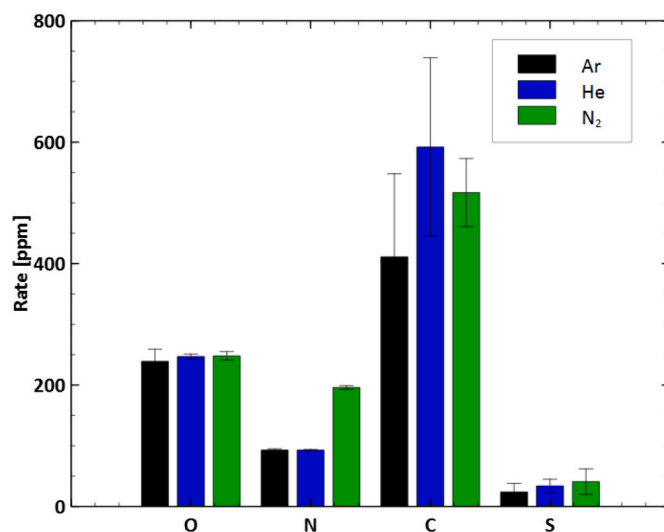


**Fig. 13.** Table: O, N, C and S contents in as-built L-PBF parts (error bars correspond to the uncertainty on the experimental measurement).
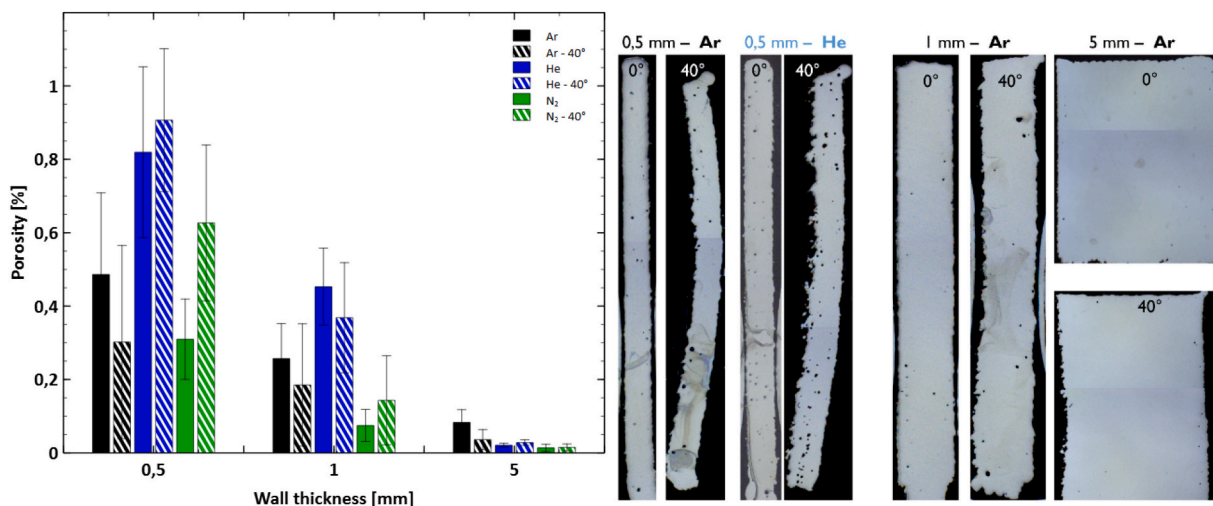


**Fig. 12.** Optical microscopy of cross sections from walls manufactured under Ar and He with three different thicknesses and two inclinations (275 W – 600 mm/s). (a) optical images of built parts, (b) influence of wall thickness, building angle and protective gas on porosity rate.
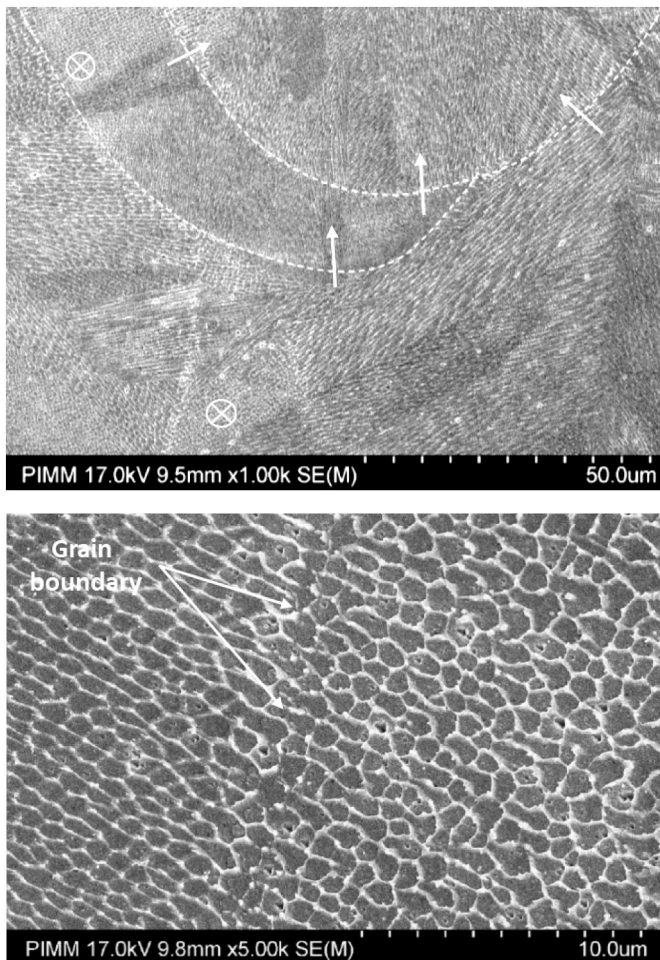
**Fig. 14.** SEM images of the microstructures of as built Inconel 625 L-PBF samples under He. Intercellular zones (enriched with Nb and Cr) are brighter than the matrix. (a) at ×1000 magnification, dendrites are mostly oriented perpendicularly to the former melt-pools edges, (b) An average 1 μm arm spacing is evidenced, whatever the gas shielding.

# 6. Influence of gaseous atmosphere on Inconel 625 microstructures

Due to the modification of thermal boundary conditions with the change of shielding gas, microstructural changes are possible, especially with helium, which promotes faster thermal dissipation and lower average temperatures in the built parts, and also with nitrogen that could be reactive with liquid nickel. To understand further the gaseous influence, various analysis were performed on samples built with the same process conditions ($P = 275$ W, $V = 0.75$ m/s, hatch distance = 120 μm, rotation angle = 33°). This includes: (1) a chemical analysis of as-built structures, (2) microstructural investigations using SEM and EBSD, (3) X-ray diffraction to identify new crystalline phases and (4) micro-hardness measurements to address mechanical properties at a local scale.

## 6.1. Chemical analysis of built parts

Chemical analysis on as built parts were carried out using an EMGA-920 non-dispersive infrared analyser, and did not point out distinct changes between O, N, C and S contents, except a factor two N enrichment of samples manufactured in $N_2$ shielding (~190 ppm versus ~85 ppm), attributed to a nitrogen dissociation and solubilization in the Inconel 625 melt-pool. Surprisingly, a small modification of the carbon

content (between 410 ppm and 590 ppm) and the sulphur content was also detected (21 ppm in Ar, 35 ppm in He and 45 ppm in $N_2$) without any clear explanation (Fig. 13).

## 6.2. SEM and EBSD microstructural analysis

At a microscale, the comparison of as built samples manufactured under Ar, He, $N_2$ did not reveal significant microstructural changes.

The solidification structure i.e. the intercellular/interdendritic distance was kept constant (Dendrite arm spacing DAS $\sim$ 1 μm) whatever the shielding gas, and Nb, Cr microsegregation in inter-cell areas was apparently not modified even if a high resolution chemical analysis would have been required to validate this point. Such data are consistent with previous works on the same alloy [21], and traduce the high solidification rate. In more detail, the orientation of dendrites mostly follows the shape of the melt-pools contours but can also be oriented perpendicularly to the investigated plane (white crosses on Fig. 14a), with a 90° tilt relative to the melt-pool boundary.

Similar solidification microstructures were also evidenced with EBSD analysis. Corresponding microstructures are typical of a keyhole (deep penetration) welding mode, with a mix of elongated and small grains oriented parallel to the build direction (BD), together with chevron-like grains normal to BD (Fig. 15). These microstructures are less columnar and less oriented (001) than those obtained on the same material by De Terris et al. [21]. This is assumed to be due to a deeper bead penetration in the current work, which promotes a larger melt-pool curvature and limits the vertical grain growth along build direction (BD). A rather low texture intensity (TI) was obtained on the three samples, with a maximum TI of 3.5 in the (111) direction under Ar. Moreover, the grain size distribution, estimated by the intercept method, was also similar, with an average diameter of ~50 μm. Last, the Kernel Average Misorientation (KAM) values considered either with the first or second neighbour pixel were analysed (Fig. 16). From these KAM data, combined with the use of a Matlab-MTEX routine, the density of geometrically necessary dislocation (GND) density $\rho_{GND}$ was calculated. The same order of magnitude for $\rho_{GND}$ (~2.9 $10^{15}$ m.m$^{-3}$ $\pm$ 0.3 $10^{15}$ m.m$^{-3}$) was obtained whatever the gas. Such values are also in phase with recent results by [21].

## 6.3. Micro-hardness tests

Micro-hardness tests (9 mm-long lines) were carried out to estimate a possible effect of gaseous atmosphere on work-hardening levels. Many factors affect hardness levels, including dislocation density, residual stresses, grain size (identical, for the three gases) or precipitation hardening (considered to be limited due to the absence of a real tempering during L-PBF). In the observed data (Fig. 17), a He shielding induces an intermediary hardness level of 279 $HV_{0.2}$, to be compared with 290 $HV_{0.2}$ with Ar and 274 $HV_{0.2}$ with $N_2$. This tends to indicate that boundary thermal conditions play a real but not dominant role in microstructure formation and resulting work-hardening levels. However, further investigations should be carried out at a more local scale to understand the reduced hardness under $N_2$, and analyse a possible precipitation substructure, including tiny γ'' ($Ni_3$ (Nb,Ti)) phases.

## 6.4. X-ray diffraction analysis

The analysis of X-ray peak widths (broadening or narrowing) can provide an interesting estimation of the amount of microstrains = work-hardening level, and of the resulting dislocation density $\rho_d$. The three X-ray diffractograms obtained on Ar, $N_2$ and He are presented in Fig. 18. Very few apparent differences are shown, except the occurrence of tiny peak for $2\theta = 54°$ and 77° for $N_2$ and He gases, not detectable with Ar. Such X-ray peaks could not be attributed with a specific crystalline phase. Another peculiarity concerns the $N_2$ diffractogram for which the amplitude of (111) peak is surprisingly lower than the amplitude of the
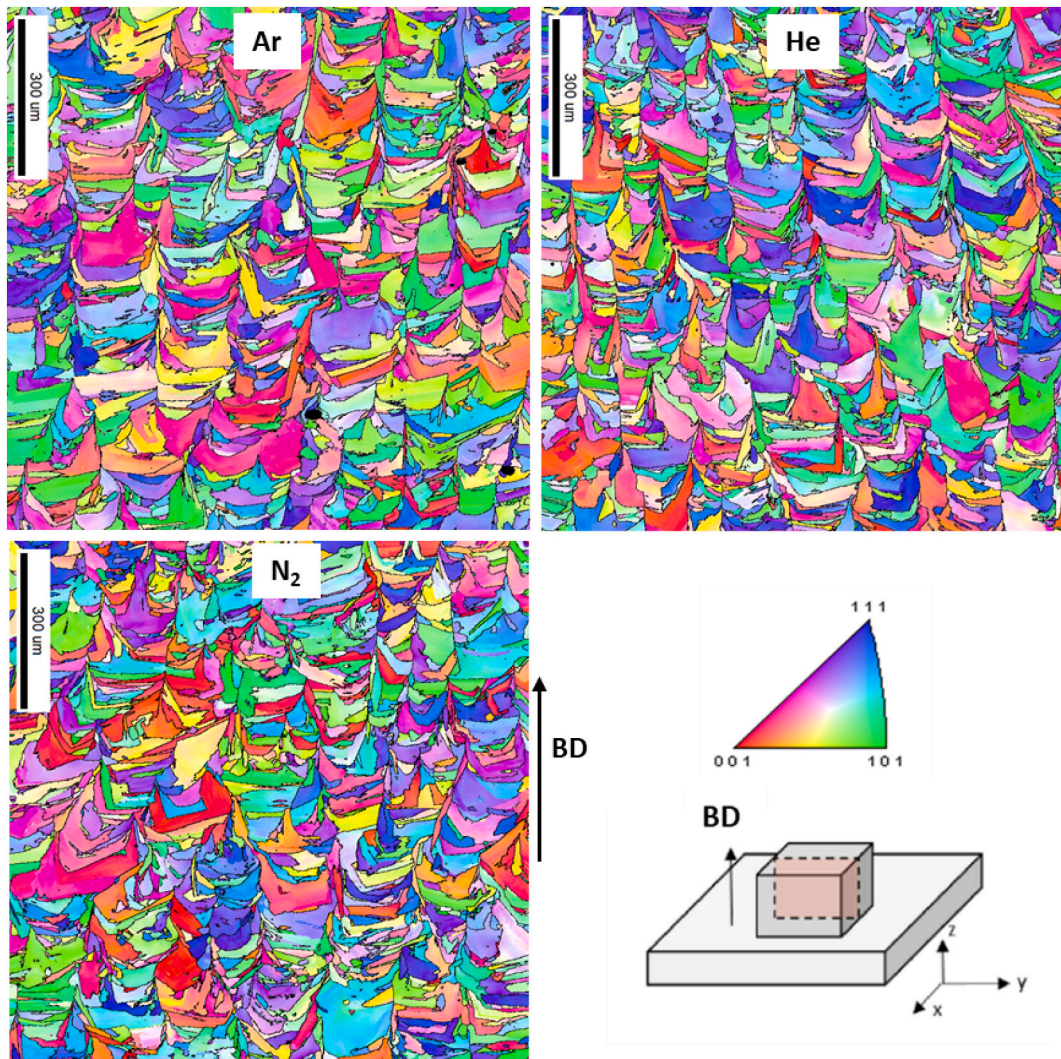
**Fig. 15.** EBSD analysis (Inverse pole figures (IPF)) on L-PBF cross-sections manufactured under Ar, He and $N_2$ shielding (BD = build direction).

(200) peak, possibly due to a texture effect.

$$\lambda = 2\, d_{hkl} sin\theta_{hkl} \tag{4}$$

With $\lambda$ = X-ray wavelength ($\lambda_{Cu}$ = 0,154,184 nm), $d_{hkl}$ = inter-reticular distance.

First, using X-ray position on I = f(2θ) diffractograms, and Bragg's law (Eq. (4)) an estimation of the lattice parameter a for a FCC material was made. Nearly similar values of a = 0.3597 nm (Ar), a = 0.3599 nm (He) and a = 0.3600 nm ($N_2$) were obtained, which indicate that the crystal distortions (induced by precipitation, residual stresses…) are nearly equivalent.

Second, an attempt was made to use four X-ray peaks of FCC Ni matrix in the 40°-100° 2θ angles range (Fig. 16) with a modified Williamson-Hall (WH) approach already used by Prasad, et al. [30]. Such an approach allows estimating the density of dislocations $\rho_d$ through an analytical analysis of x-ray peak broadening (for more information about the WH calculation, please refer to [21,30]. However, and even with the use of specific contrast factors for dislocations on (111), (200), (220) and (311) planes, obtained results were too scattered to be really convincing, especially on $N_2$. A rough estimation of $\rho_d$ only exhibited values in the $5.10^{14}$–$5.10^{15}$ m.m$^{-3}$ range, without clear distinction between the three gaseous atmospheres.

## 7. Discussion

Very few studies have considered already the use of a large range of gas properties in the L-PPBF process. In the current work, with a specific focus on surface topography, porosity rate and microstructures of an Inconel 625, different and sometimes contradictory effects have been evidenced.

Compared with a classical argon protection, helium globally induces a better process stability:

- It promotes heat dissipation and favours smoothing of edge surfaces by limiting the wall surface temperature, and the number of agglomerated particles, except for undercut surfaces built with a 40° angle for which surfaces are strongly deteriorated, with a melt-pool tendency to overflow under the action of gravity forces. This unexpected result (roughness of L-PBF parts usually increases with wall temperatures and high P/V values) seems contradicted by the lower distorsions of thin walls under helium (Fig. 12b), attributed to a better heat dissipation in a highly conductive gas. An assumption would be that stronger heat accumulation under Ar (higher T) could induce lower ρ values and slightly lighter (=more stable) melt-pools in overhang position. However this seems rather unlikely.
- Helium improves the surface roughness of build surfaces (perpendicular to the build direction), and favours liquid spreading between adjacent beads.
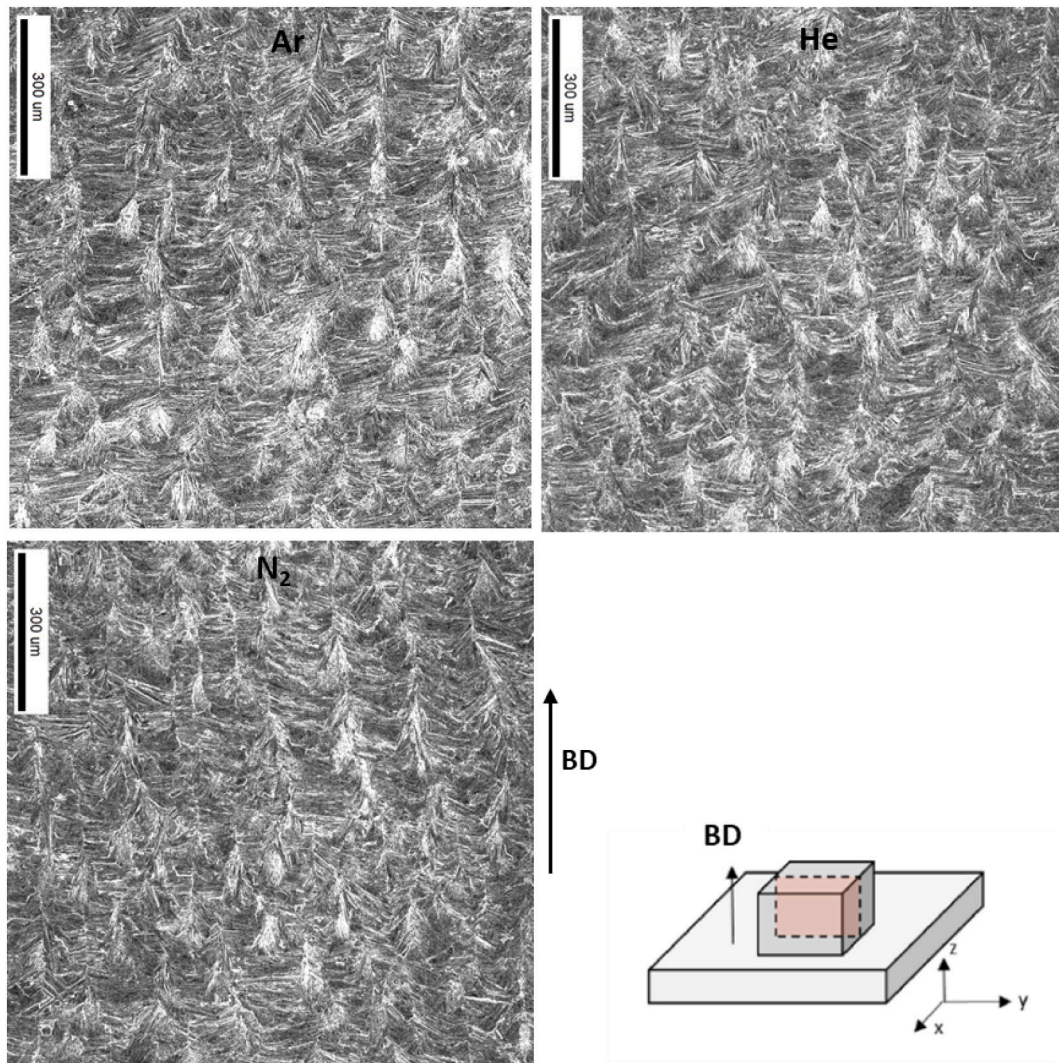
**Fig. 16.** Kernel Average Misorientation (KAM) for Ar, He and $N_2$ shielding (BD = build direction), misorientation angle range = $0°$ (black) to $1°$ (white).

At first sight, the better liquid spreading, and smaller menisci shown in Fig. 8 could be attributed to a reduction of surface tensions between liquid Inconel 625 and helium. However, tensio-active effects are usually dependent on the chemical content of the melt-pool, which does not vary significantly with helium, still considered as a neutral gas. This is confirmed experimentally by Sarou-Kanian et al. [31] on aluminum, where both Ar and He protective gas induce the same surface tensions $\gamma_{LV}$. To explain the observed results, one could assume a local modification of the $O_2$ content near the built samples, especially considering the high helium flow rate (10 m/s) compared with argon (2.8 m/s).

- It also reduces the number of spatters (Fig. 8), which result has already been shown in [17].

To explain the reduction of spattering under He, Traore et al. [17] claimed that due to a faster vertical expansion of the vapour plume, resulting in larger denudation effects, small powder particles were more easily incorporated in the melt-pool by the lateral dragging force, and less ejected-entrained by the vapour plume. This incorporation could also be favoured by a reduction of surface tension. On the other hand, the larger spatters (>100 μm) come from a destabilization of the melt-pool when the kinetic energy of the melt-pool flow ($\sim \rho\ V_{MP}^2$) exceeds local surface tension forces ($\gamma_{LV}/r$). In that case, larger liquid/gas surface tensions would promote a reduction of large spatters by stabilizing the melt-pool.

- Even though porosity levels are low (<0.25 %), helium tends to reduce porosity (Fig. 11), especially at high VED (96 J/mm³) corresponding to the deeper melt-pools.

Many factors can influence this effect: (1) a better solubilization of small helium atoms in liquid metal, (2) a better melt-pool and/or keyhole front wall stability during keyhole fusion, (3) lower surface tensions promoting porosity escape from melt-pools.

The influence of nitrogen ($N_2$) shielding is moderate compared with helium:

- It reduces slightly the density of pores for large VED/large parts (Fig. 11) and thin walls at constant VED (Fig. 12). Such a result agrees partially with results from Kuo et al. [9] on Inconel 690 in keyhole welding conditions, who observed a strong reduction of porosity under $N_2$. Such an effect, attributed by Kuo et al. [9] to a reduction of surface tension that favours pore dissolution and a higher solubility of N in Cr-rich liquids, is not dominant in the current work.
- It does not modify surface roughness (Fig. 7) and process stability (Fig. 8)
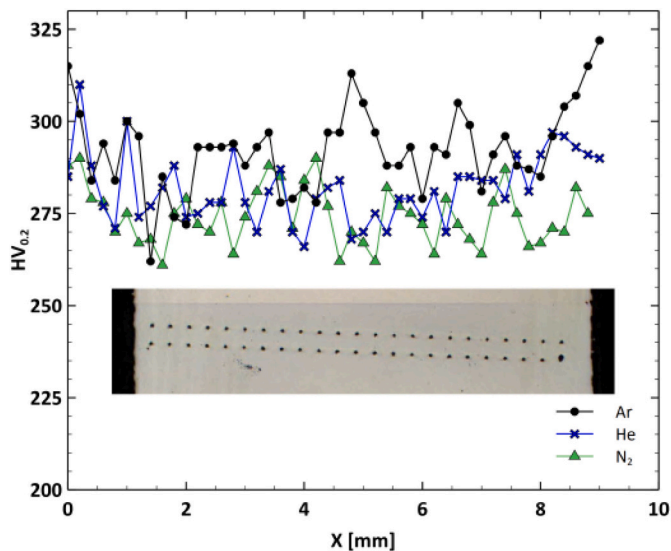
**Fig. 17.** Vickers Hardness tests (200 gf) on top built surface (0° build angle) of squared samples. Average Hardness values are as follows: 290 $HV_{0.2}$ (Ar, black), 279 $HV_{0.2}$ (He, blue), 274 $HV_{0.2}$ ($N_2$ green). (For interpretation of the references to colour in this figure legend, the reader is referred to the web version of this article.)
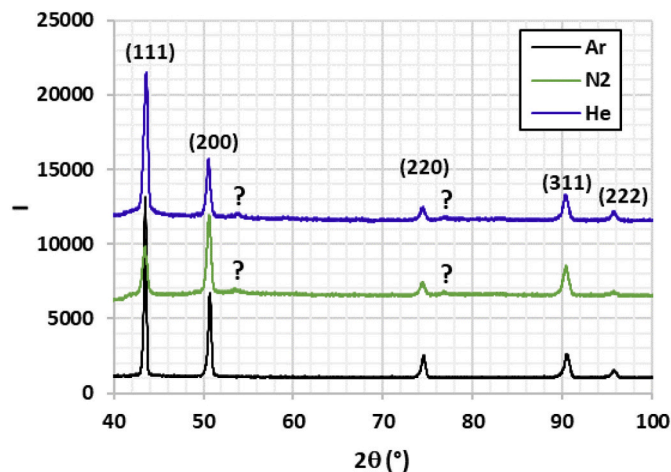


**Fig. 18.** X-ray diffraction profiles (I = f (2θ) angle) for Ar, $N_2$, He.

Consequently, a surfactant effect of solubilized nitrogen in the Inconel 625 melt-pool is possible, but without significant effect on roughness and laser/melt-pool interaction.

Considering all these data, a clear physical understanding of the influence of shielding gas on Inconel 625 melt-pools for L-PBF in keyhole mode still remains complex, and needs to be considered with caution.

In a second step, microstructures and local mechanical properties (hardness) were investigated in order to check a possible influence of cooling effects (with helium) and of a slightly modified chemical composition (with $N_2$).

Globally, a moderate influence of the gas shielding on as-built microstructures was shown, at least at the micro-scale considered in the current work. However, a tiny reduction of hardness values was evidenced with He and $N_2$. This result was compared with X-ray diffraction (XRD) analysis of L-PBF samples, which indicates a larger peak broadening with Ar samples than with the two other gases. A Williamson-Hall analysis of peak-broadening, already used by De Terris et al. [21] and Prasad et al. [30] was carried out, and allowed a rough estimation of dislocation densities, with $\rho_d$ comprised between $5.10^{14}$ and $5.10^{15}$ m.

$m^{-3}$. However, such data, taking into account all the contributions of statistically stored dislocations (SSD) were much too scattered, and not confirmed by the KAM analysis and the estimation of geometrically necessary dislocations (GND). This latter KAM analysis did not evidence any clear difference between the three gases with an average estimated value of $\rho_{GND} = 2.9.10^{15}$ m.m.$^{-3}$.

A more detailed analysis of dislocation structure using TEM should be performed to confirm or infirm these preliminary data, and the possible reduction of L-PBF thermal work-hardening in a high conductive gas through a decrease of dislocation density. Another interesting work to be done would be to analyse the influence of part size on the L-PBF thermally induced work-hardening. Such an influence was clearly shown by Bertsch, et al. [32] who indicated that dislocation density increased in a L-PBF 316L steel with increasing constraints (i.e. larger built volume) surrounding the melt-pool. However, in the current work, no size influence was shown on microhardness values, and it was not possible to analyse thin walls with X-ray diffraction, due to the large diameter of the X-ray spot (around 2.5 mm).

## 8. Conclusion

The influence of three protective gases (argon, helium and nitrogen) on surface finish, porosity rate, and microstructures of Inconel 625 L-PBF samples were considered. Based on the dimensions of fusion zones, the laser-matter energy coupling was not widely modified by the gas change, but the use of a high thermal conductivity gas like helium was shown to improve surface roughness, and to limit thermal distortions on thin samples, due to a better heat dissipation. Nearly similar porosity rates were obtained whatever the building angle, and the protective gas, except for high input energy where benefits were shown for He and $N_2$. The modification of surface tensions at the melt-pool/gas interface was considered as a hypothetical contribution to the change of surface finish. Last, no significant microstructural change was shown with the change of gas. However, this should be confirmed with further microstructural analysis at a more microscopic scale.

## Declaration of competing interest

The authors declare that they have no known competing financial interests or personal relationships that could have appeared to influence the work reported in this paper.

## References

[1] Colopi M, Demir AG, Caprio L, Previtali B. Limits and solutions in processing pure Cu via selective laser melting using a high-power single-mode fiber laser. Int J Adv Manuf Technol 2019;104(5–8):2473–86. https://doi.org/10.1007/s00170-019-04015-3.

[2] Bidare P, Maier RJ, Beck RJ, Shephard JD, Moore AJ. An open-architecture metal powder bed fusion system for in-situ process measurements. Addit Manuf 2017;16: 177–85. https://doi.org/10.1016/j.addma.2017.06.007.

[3] Matthews MJ, Guss G, Khairallah SA, Rubenchik AM, Depond PJ, King WE. Denudation of metal powder layers in laser powder bed fusion processes. Acta Mater 2016;114:33–42. https://doi.org/10.1016/j.actamat.2016.05.017.

[4] Bidare P, Bitharas I, Ward RM, Attallah MM, Moore AJ. Laser powder bed fusion in high-pressure atmospheres. Int J Adv Manuf Technol 2018;99(1-4):543–55. https://doi.org/10.1007/s00170-018-2495-7. ISSN : 0268-3768, 1433-3015.

[5] Wang D, Wu F, Fu S, Mai S, Yang Y, Liu Y, Song C. Mechanisms and characteristics of spatter generation in SLM processing and its effect on the properties. Mater Des 2017;117:121–30. https://doi.org/10.1016/j.matdes.2016.12.060. 02641275.

[6] Gunenthiram V, Peyre P, Schneider M, Dal M, Coste F, Koutiri I, Fabbro R. Experimental analysis of spatter generation and melt-pool behavior during the powder bed laser beam melting process. J Mater Process Technol 2018;251: 376–86. https://doi.org/10.1016/j.jmatprotec.2017.08.012.

[7] Zhao C, Fezzaa K, Cunningham RW, Wen H, De Carlo F, Chen L, Rollett AD, Sun T. Real-time monitoring of laser powder bed fusion process using high-speed X-ray imaging and diffraction. Sci Rep 2017;7:3602. 10.1038, s41598-017-03761-2.

[8] Greses J, Hilton PA, Barlow CY, Steen WM. Plume attenuation under high power Nd:yttritium–aluminum–garnet laser welding. J Laser Applic 2004;16.1(fév. 2004): 9–15. https://doi.org/10.2351/1.1642636.

[9] Kuo TY, Lin YD. Effects of different shielding gases and power waveforms on penetration characteristics and porosity formation in laser welding of Inconel 690 alloy. Mater Trans 2007;48(2):219–26. https://doi.org/10.2320/matertrans.48.219.

[10] Patschger A, Sahib C, Bergmann JP, Bastick A. Process optimization through adaptation of shielding gas selection and feeding during laser beam welding. PhysProcedia 2011;12:46–55. https://doi.org/10.1016/j.phpro.2011.03.007.

[11] Rakesh S, Priyank N, Vasa NJ. Effect of build atmosphere on the mechanical properties of AlSi10Mg produced by selective laser melting. Mater Today 2018;5: 17231–8.

[12] Ferrar B, Mullen L, Jones E, Stamp R, Sutcliffe CJ. Gas flow effects on selective laser melting (SLM) manufacturing performance. J Mater Process Technol 2012; 212(2):355–64. https://doi.org/10.1016/j.jmatprotec.2011.09.020.

[13] Anwar AB, Pham QC. Selective laser melting of AlSi10Mg: effects of scan direction, part placement and inert gas flow velocity on tensile strength. JMaterProcessTechnol 2017;240:388–96. https://doi.org/10.1016/j.jmatprotec.2016.10.015. 09240136.

[14] Reijonen J, Revuelta A, Riipinen T, Ruusuvuori K, Puukko P. On the effect of shielding gas flow on porosity and melt pool geometry in laser powder bed fusion additive manufacturing. Addit Manuf 2020;32:101030. https://doi.org/10.1016/j.addma.2019.101030.

[15] Wang XJ, Zhang LC, Fang MH, Sercombe TB. The effect of atmosphere on the structure and properties of a selective laser melted Al–12 Si alloy. MaterSciEngA 2014;597:370–5. https://doi.org/10.1016/j.msea.2014.01.012.

[16] Dai D, Gu D. Effect ofmetal vaporization behavior on keyhole-mode surface morphology of selective laser melted composites using different protective atmospheres. Appl Surf Sci 2015;355:310–9. https://doi.org/10.1016/j.apsusc.2015.07.044.

[17] Traore S, Schneider M, Koutiri I, Coste F, Fabbro R, Charpentier C, Lefebvre P, Peyre P. Influence of gas atmosphere (argon or helium) on the laser powder bed fusion of a Ni-based alloy. J Mater Process Technol 2021;288:116851. https://doi.org/10.1016/j.jmatprotec.2020.116851.

[18] Mayi YA, Dal M, Peyre P, Bellet M, Metton C, Moriconi C, Fabbro R. Laser-induced plume investigated by finite element modelling and scaling of particle entrainment in laser powder bed fusion (LPBF). JPhysDApplPhys 2019;1361–6463. https://doi.org/10.1088/1361-6463/ab5900.

[19] Pauzon C, Foret P, Hryha E, Arunprasad T, Nyborg L. Argon-helium mixtures as laser-powder bed fusion atmospheres: towards increased build rate of Ti-6Al-4V. JMaterProcessTechnol 2020;279:116555.

[20] Fabbro R. Scaling laws for the laser welding process in keyhole mode. J Mater Process Technol 2019;264:346–51. https://doi.org/10.1016/j.jmatprotec.2018.09.027.

[21] De Terris T, Castelnau O, Hamouche Z, Haddadi H, Michel V, Peyre P. Analysis of as-built microstructures and recrystallization phenomena on Inconel 625 alloy obtained by laser powder bed fusion (L-PBF). Metals 2021;11:619. https://doi.org/10.3390/met11040619.

[22] Strano G, Hao L, Everson RM, Evans KE. Surface roughness analysis, modelling and prediction in selective laser melting. J Mater Process Technol 2013;213.4:589–97. https://doi.org/10.1016/j.jmatprotec.2012.11.011. 09240136.

[23] Air Liquide. Encyclopédie Des Gaz Encycl. Gaz. https://encyclopedia.airliquide.com/fr; 2020. ISSN : 0268-3768, 1433-3015.

[24] Liu Y, Zhang J, Yang Y, Li J, Chen J. Study on the influence of process parameters on the clearance feature in non-assembly mechanism manufactured by selective laser melting. J Manuf Process 2017;27:98–107. https://doi.org/10.1016/j.jmapro.2017.04.005. 15266125.

[25] Koutiri I, et al. Influence of SLM process parameters on the surface finish, porosity rate and fatigue behavior of as-built Inconel 625 parts. J Mater Process Technol 2018;255:536–46. https://doi.org/10.1016/j.jmatprotec.2017.12.043.

[26] Yan X, Gao S, Chang C, Huang K, Khanlari K, Dong D, Ma W, Fenineche N, Liao H, Liu M. Effect of building directions on the surface roughness, microstructure, and tribological properties of selective laser melted Inconel 625. J Mater Process Technol 2021;288:116878.

[27] Ladewig A, Schlick G, Fisser M, Schulze V, Glatzel U. Influence of the shielding gas flow on the removal of process by-products in the selective laser melting process. Addit Manuf 2016;10:1–9. https://doi.org/10.1016/j.addma.2016.01.004.

[28] Tang M, Pistorius PC, Beuth JL. Prediction of lack-of-fusion porosity for powder bed fusion. Addit Manuf 2017;14:39–48. https://doi.org/10.1016/j.addma.2016.12.001. 22148604.

[29] Shrestha S, Chou K. Formation of keyhole and lack of fusion pores during the laser powder bed fusion process. ManufLett 2022;32:19–23. https://doi.org/10.1016/j.mfglet.2022.01.005.

[30] Prasad K, Obana M, Ito A, Torizuka S. Synchrotron diffraction characterization of dislocation density in additively manufactured IN 718 superalloy. Mater Charact 2021;179:111379.

[31] Sarou-Kanian V, Millot F, Rifflet JC. Surface tension and density of oxygen-free liquid aluminum at high temperature. IntJThermophys 2013;24(1). https://doi.org/10.1023/A:1022466319501.

[32] Bertsch KM, Meric de Bellefon G, Kuehl B, Thoma DJ. Origin of dislocation structures in an additively manufactured austenitic stainless steel 316L. Acta Mater 2020;199:19–33.